International Journal of Solids and Structures 47 (2010) 2316–2327

Contents lists available at ScienceDirect

International Journal of Solids and Structures

journal homepage: www.elsevier.com/locate/ijsolstr

Prediction of plane strain fracture of AHSS sheets with post-initiation softening

Yaning Li, Tomasz Wierzbicki *

Massachusetts Institute of Technology, #77 Massachusetts Avenue, Room 5-218, Cambridge, MA 02139, United States

ARTICLE INFO

Article history:
Received 16 October 2009
Received in revised form 27 April 2010
Available online 22 May 2010

Keywords:
Post-initiation
Softening
Ductile fracture
AHSS
Slant fracture

ABSTRACT

In this investigation, the three-parameter Modified Mohr–Coulomb (MMC) fracture model and the determination of the material parameters are briefly described. The formulation of the post-initiation behavior is proposed by defining both the explicit softening law and the incremental damage evolution law. As opposed to the existing attempts to simulate slant fracture with material weakening before crack formation, softening is assumed to occur only in the post-initiation range. The justification of this assumption can be provided by the interrupted fracture tests, for example, Spencer et al. (2002).

Element deletion with a gradual loss of strength is used to simulate crack propagation after fracture initiation. The main emphasis of the paper is the numerical prediction of slant fracture which is almost always observed in thin sheets. For that purpose, VUMAT subroutines of ABAQUS are coded with post-initiation behavior for both shell elements and plane strain elements. Fracture of flat-grooved tensile specimens cut from advanced high strength steel (AHSS) sheets are simulated by 2D plane strain element and shell element models.

1. Introduction

Ductile fracture strongly depends on the microstructures of the material, voids, inclusions and micro cracks. Usually, ductile fracture is viewed as the result of void nucleation, growth and coalescence. Generally, there are two different types of approaches in the literature to capture this process. In the first approach fracture is modeled as a process of damage accumulation within the continuum, which means the constitutive model and fracture model are coupled. In the second approach, fracture is considered as a sudden event when the stress and strain states of the undamaged continuum reaches a critical level. For convenience, the former type is referred to as *coupled fracture modeling* and the latter as *uncoupled fracture modeling.* Both of them have both advantages and disadvantages.

Coupled fracture model is a natural extension of the concept of continuum damage mechanics (CDM), originally introduced by Kachanov (1958) and then further developed by Hult (1979), Chaboche (1981), Krajcinovic (1984), Lemaitre (1985) and others. CDM treats damage as an internal state variable in the framework of thermodynamics (e.g. Coleman and Gurtin, 1967; Rice, 1971) and involves averaging of the effect of damage into the constitutive relations. Fracture occurs when the damage accumulation reaches a critical value. Some models introduce damage right into the yield surface. An example is the classic Gurson model (Gurson, 1975, 1977) for porous material. It includes the porosity in the yield function with a linear incremental evolution law. Thus the average effects of porosity induced damage are built into the constitutive model. An alternative approach is to introduce damage into the hardening law, which belongs to a type of damage-induced softening (Teng, 2008; Xue, 2007). The *coupled fracture modeling* is physically realistic and it can capture slant fracture, Besson et al. (2001, 2003). But the calibration effort is great. For example, nine parameters need to be calibrated when Gurson or Rousselier type model is used to simulate fracture (Teng, 2008).

The prototype of the uncoupled fracture model is the McClintock (1968) model which demonstrates that the fracture strain is related to the stress state and the geometry of the voids. Rice and Tracey (1969) proposed a void growth model to show how stress-states affect voids growth. Ductile fracture usually occurs in the stage of sustained plastic flow. The hardening curve flattens at larger strain, stress has lower resolution than strain. Therefore, it is more convenient to use the strain rather than the stress-based criteria to simulate ductile fracture. Bao and Wierzbicki (2004a,b, 2005) determined a fracture locus in a wide range of stress triaxiality based on the results of 36 meticulous experiments and numerical simulation of several kinds of specimens and loading cases including solid cylinders, square bars, thin sheets and plates with holes. More recently, a general form of asymmetric metal plasticity, considering both the pressure sensitivity and the Lode dependence, was postulated by Bai and Wierzbicki (2008). Also, a new 3D asymmetric fracture locus, in the space of equivalent fracture strain, stress triaxiality and the Lode angle parameter, was postulated by Bai (2008) and Bai and Wierzbicki (2010), as an extension of Mohr–Coulomb (M_C) failure criterion. Since the de-

* Corresponding author. Tel.: +1 617 253 2104.
E-mail address: wierz@mit.edu (T. Wierzbicki).

0020-7683/$ - see front matter © 2010 Elsevier Ltd. All rights reserved.
doi:10.1016/j.ijsolstr.2010.04.028

tails of the mechanism of void growth are not explicitly involved into the fracture calibration methodology, fewer parameters are needed to be calibrated from experiments. This is less expensive and more straightforward. Most importantly, good correlations of predicted load–displacement curve and experimental data can be obtained, which makes this approach quite promising for industry application. However, the details of the fracture modes can not be captured accurately by this approach. For example, with the hardening rule and no damage-induced softening, the slant fracture mode can not be predicted by the FE simulations.

In this paper, a semi-coupled approach is used to combine the advantages of both coupled and uncoupled models. The equivalent strain to failure is calibrated from the three-parameter Modified Mohr–Coulomb (MMC) criterion and the damage-induced softening is introduced in the post-initiation range. The increment of damage is proportional to the increment of plastic strain. Similar as the CDM approach, the damage accumulates from the very beginning, but weakening of the hardening curve is activated after damage reaches a critical value. When implementing this approach to the FEM simulation, the fracture initiates in the element after the locus of equivalent plastic strain to failure is reached and the softening is shut on in the post-initiation process and the element will not be deleted until the damage accumulates to a critical value. In this way, it is expected that both the accurate critical displacement to fracture and the slant fracture mode can be captured.

As an application and validation of this approach developed in Sections 2 and 3, VUMAT subroutines of ABAQUS is coded with post-initiation behavior for both shell element and plane strain element. The plane strain element models are used in Section 4 to predict the fracture of flat-grooved tensile specimen of AHSS sheets. Factors influencing the prediction of the slant fracture are studied. Results of shell element model are discussed and compared with the plane strain element model and the experimental data in Section 5.

2. MMC fracture model and calibration

2.1. Definition of stress state variables

Denote the stress tensor $\underline{\sigma}$ with three ordered components in the principle directions by σ_1, σ_2 and σ_3. The first invariant of the stress tensor is

$$\sigma_m = \frac{1}{3} Tr(\underline{\sigma}) = \frac{1}{3}(\sigma_1 + \sigma_2 + \sigma_3). \tag{1}$$

The second and the third invariants of the deviatoric stress tensor $\underline{S}$, denoted respectively by $\bar{\sigma}$ and r are

$$\bar{\sigma} = \sqrt{\frac{3}{2}\underline{S} : \underline{S}} = \sqrt{\frac{1}{2}\left[(\sigma_1 - \sigma_2)^2 + (\sigma_2 - \sigma_3)^2 + (\sigma_1 - \sigma_3)^2\right]}, \tag{2}$$

$$r = \left(\frac{9}{2}\underline{S} \cdot \underline{S} : \underline{S}\right)^{\frac{1}{3}} = \left[\frac{27}{2}(\sigma_1 - \sigma_m)(\sigma_2 - \sigma_m)(\sigma_3 - \sigma_m)\right]^{\frac{1}{3}}. \tag{3}$$

The triaxiality parameter is defined in a usual way:

$$\eta = \frac{\sigma_m}{\bar{\sigma}}. \tag{4}$$

An important feature of the Mohr–Coulomb failure criterion is that it depends on the Lode angle parameter $\bar{\theta}$, which is related to the normalized third stress invariant by

$$\bar{\theta} = 1 - \frac{2}{\pi}\arccos\left(\left(\frac{r}{\bar{\sigma}}\right)^3\right). \tag{5}$$

Two special cases will be of interest to the present investigation: plane stress and the plane strain. The reader is referred to Fig. 1 which defines the coordinate system used for thin sheets.

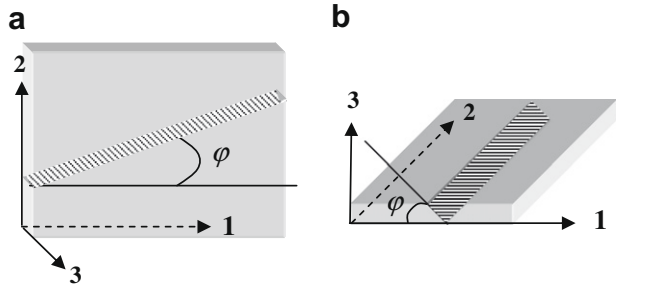

Fig. 1. Coordinates in the plane stress and plane strain conditions and orientations of fracture planes. (a) Plane stress with $\sigma_3 = 0$. (b) Plane strain with $\dot{\varepsilon}_2 = 0$.

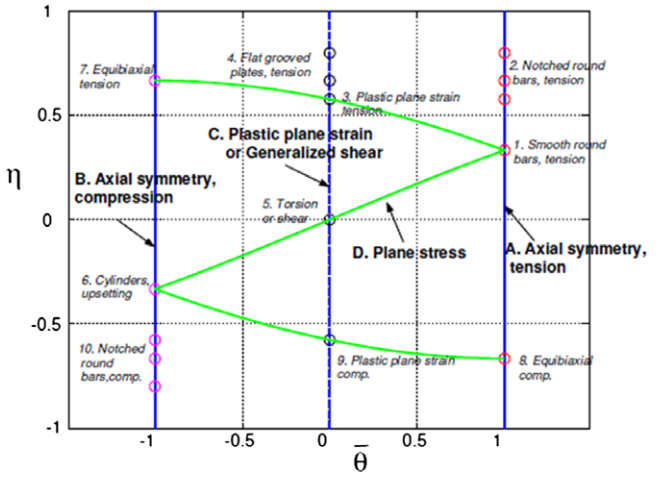

Fig. 2. Initial stress-states on the plane of $(\bar{\theta}, \eta)$ (Bai and Wierzbicki, 2008).

For the plane stress condition (see Fig. 1a), $\sigma_3 = 0$. By substituting it into Eqs. (2), (3) and (5), the triaxiality and Lode parameter are related through (Wierzbicki and Xue, 2005; Bai and Wierzbicki, 2008):

$$-\frac{27}{2}\eta\left(\eta^2 - \frac{1}{3}\right) = \sin\left(\frac{\pi}{2}\bar{\theta}\right). \tag{6}$$

This relation is illustrated in Fig. 2, showing various stress-states in different types of tests.

In the case of plane strain, $\dot{\varepsilon}_2 = 0$ (see Fig. 1b). Following the definition of $\bar{\theta}$, and the associated flow rule, in the case of plane strain, $\bar{\theta} = 0$. If both plane stress and plane strain prevails under tension, then $\eta = \frac{1}{\sqrt{3}}$ and $\bar{\theta} = 0$, as shown in Fig. 2.

2.2. Fracture model

The prediction of plane strain fracture is based on the three-parameter Modified Mohr–Coulomb criterion (Eq. (7)) for power law isotropic hardening material:

$$\max(\tau + C_1\sigma_n) = C_2, \tag{7}$$

where τ and σ_n are the shear and normal stress acting at a given plane and C_1 and C_2 are material constants. Fracture is said to occur at a plane in which the left hand side of Eq. (7) is maximized. It was shown by Bai (2008) and Bai and Wierzbicki (2010) that in the case of plane stress, the fracture plane is inclined to the major principal axis 1 by angle φ, see Fig. 1a. In the plane strain case, the fracture plane is slant with respect to the thickness direction, see Fig. 1b. The angle φ is uniquely related to the constant C_1 by

$$\cos^2\varphi = \frac{1}{1 + \left(\sqrt{1 + C_1^2} + C_1\right)^2}. \tag{8}$$

Even though the MMC stress-based fracture model has a simple interpretation and involves only two free parameters, its direct application is limited. The main reason is that stresses and in particular, stress at the point of fracture can not be measured directly from the tests. Therefore, there is a need to transform the stress-based fracture model into the corresponding strain-based model. This was done by Bai (2008) and Bai and Wierzbicki (2010) using the power hardening rule in conjunction with non-quadratic yield condition:

$$\bar{\sigma} = A\bar{\varepsilon}^n \left\{ C_3 + \frac{\sqrt{3}}{2-\sqrt{3}}(1-C_3)\left(\sec\frac{\pi\bar{\theta}}{6} - 1\right)\right\}, \tag{9}$$

where n is the hardening exponent, A is the amplitude and $\bar{\varepsilon}$ is the equivalent strain. The parameter C_3 is responsible for the yield surface. For example, $C_3 = 1$ would correspond to the Von Mises yield condition; while $C_3 = \frac{\sqrt{3}}{2}$ will give the Tresca yield condition. The intermediate values of this parameter define a family of yield loci, similar to the exponent of the non-quadratic yield condition (Hosford, 1972). In this way, the shape of the yield curve can be made more precise to transform the fracture criterion from the stress space to the mixed space. For a more detailed explanation of the role of the parameter C_3, the reader is referred to the recently published paper by Bai and Wierzbicki (2010).

The local MMC criterion can be expressed in terms of all three stress invariants. Then, expressing the equivalent stress in terms of the equivalent strain, the final expression of the modified MMC criterion takes the form:

$$\bar{\varepsilon}_f(\eta,\bar{\theta}) = \left\{ \frac{A}{C_2}\left[C_3 + \frac{\sqrt{3}}{2-\sqrt{3}}(1-C_3)\left(\sec\left(\frac{\bar{\theta}\pi}{6}\right) - 1\right)\right] \times \left[\sqrt{\frac{1+C_1^2}{3}}\cdot\cos\left(\frac{\bar{\theta}\pi}{6}\right) + C_1\left(\eta + \frac{1}{3}\sin\left(\frac{\bar{\theta}\pi}{6}\right)\right)\right]\right\}^{\frac{1}{n}}. \tag{10}$$

The reader refers to Bai and Wierzbicki (2010) for details of the derivation of Eq. (10). The equivalent strain to failure $\bar{\varepsilon}_f$ is seen to be the function of stress triaxiality η and Lode angle parameter $\bar{\theta}$. Now there are three material fracture constants C_1, C_2 and C_3 to be determined from tests. In the limiting case of plane stress, Eq. (10) reduces to:

$$\bar{\varepsilon}_f(\eta,\bar{\theta}) = \left\{ \frac{A}{C_2} f_3 \left[\sqrt{\frac{1+C_1^2}{3}}\cdot f_1 + C_1\left(\eta + \frac{f_2}{3}\right)\right]\right\}^{\frac{1}{n}}, \tag{11}$$

where,

$$f_1 = \cos\left\{\frac{1}{3}\arcsin\left[-\frac{27}{2}\eta\left(\eta^2 - \frac{1}{3}\right)\right]\right\}, \tag{12}$$

$$f_2 = \sin\left\{\frac{1}{3}\arcsin\left[-\frac{27}{2}\eta\left(\eta^2 - \frac{1}{3}\right)\right]\right\}, \tag{13}$$

$$f_3 = C_3 + \frac{\sqrt{3}}{2-\sqrt{3}}(1-C_3)\left(\frac{1}{f_1} - 1\right). \tag{14}$$

In the case of plane strain, the three-parameter Modified Mohr–Coulomb criterion takes the simpler form:

$$\bar{\varepsilon}_f(\eta,\bar{\theta}) = \left\{ \frac{AC_3}{C_2}\left[\sqrt{\frac{1+C_1^2}{3}} + C_1\eta\right]\right\}^{\frac{1}{n}}. \tag{15}$$

This concludes a short summary of the present fracture theory. The method proposed in this paper will be illustrated on the example of TRIP[1] 690 steel, which is one product of ThyssenKrupp[2] in the category of the advanced high strength steel (AHSS), grade (ThyssenKrupp Auto Division-Product Overview, 2008): RA-K 40/70, standard HCT690T. Also, it is cold rolled retained austenite steel with 690 MPa minimum tensile strength. The plasticity and fracture parameters (C_1, C_2 and C_3) of this steel were determined by Bai and Wierzbicki (2010). It was found that $A = 1275.9$ MPa, $n = 0.2655$, $C_1 = 0.12$, $C_2 = 720$ MPa, $C_3 = 1.095$. The hardening curve is shown in Fig. 3a. Five calibration tests and the corresponding experimental points are shown in Fig. 3b. Readers are referred to Bai and Wierzbicki (2010) for details of various test specimens. The calibration process is similar to that described by Beese et al. (2010) for Al6061-T6.

According to Eq. (10), the fracture envelope forms a 3D surface in the space of the equivalent strain to fracture, triaxiality and Lode parameter, as shown in Fig. 4a. The general fracture envelope can be mapped into the 2-D space of triaxiality and equivalent strain to fracture in the cases of plane stress and plane strain, as shown in Fig. 4b.

2.3. Test program

A limited test program was conducted on the flat-grooved tensile specimens cut at 0°, 45° and 90° to the rolling direction. The dimensions of the specimens are shown in Fig. 5. The tensile tests were performed in a displacement controlled MTS loading frame.The load–displacement histories during tension were recorded and shown with the photos of speciments in Fig. 6. The in-plane components of the strain tensor just before fracture were measured by the digital image correlation (DIC) system and converted from the Lagrangian to logarithmic measures. The out-of-plane component of the strain tensor was also measured through thickness reduction. For the isotropic material, the relation between the logarithmic through thickness strain and the equivalent strain is given by $\bar{\varepsilon}_f = \frac{2}{\sqrt{3}}\ln\left(\frac{t_0}{t_f}\right)$, where t_0 and t_f are the initial and final thicknesses respectively. The TRIP 690 steel sheets were shown by Bai and Wierzbicki (2010) to exhibit little anisotropy in both plasticity and fracture properties. This observation in plasticity is confirmed by the present experiments where the load–displacement curves for specimens cut in three directions were close to each other. However, there is a difference in fracture displacements, depending on the orientations of the material, as shown in Fig. 6. This discrepancy is due to the machining of the grooved surfaces of the specimens. Since it is an unexpected distraction form the present topic, in the FE simulations, this machining-induced anisotropy is neglected.

From Fig. 6, it can also be seen that catastrophic failure occurs and the crack propagation is unstable. It has to be noted that the fracture surfaces of all specimens are slant through thickness, as revealed from the cut and polished section of the specimens.

3. Post-initiation behavior

An interesting insight into the plane strain fracture process was provided by Spencer et al. (2002). They conducted interrupted tests and found that a central void is formed from which the fracture surface slantingly propagates to the edge of the specimen causing total separation. Spencer's interrupted tests (2002) showed the general mechanism of damage evolution and the formation of slant fracture in the post-initiation process. The interrupted tests are very time consuming and therefore were not conducted for the present project dealing with the TRIP 690.

It is also shown by Spencer et al. (2002) that the post-initiation behavior is a material property and its range increases with the ductility of the material, see Fig. 7. It is found by Hutchinson and Tvergaard (1981) that for a material with a smooth yield surface

[1] TRIP, transformation induced plasticity.
[2] ThyssenKrupp Steel Europe AG, Duisburg, Germany.

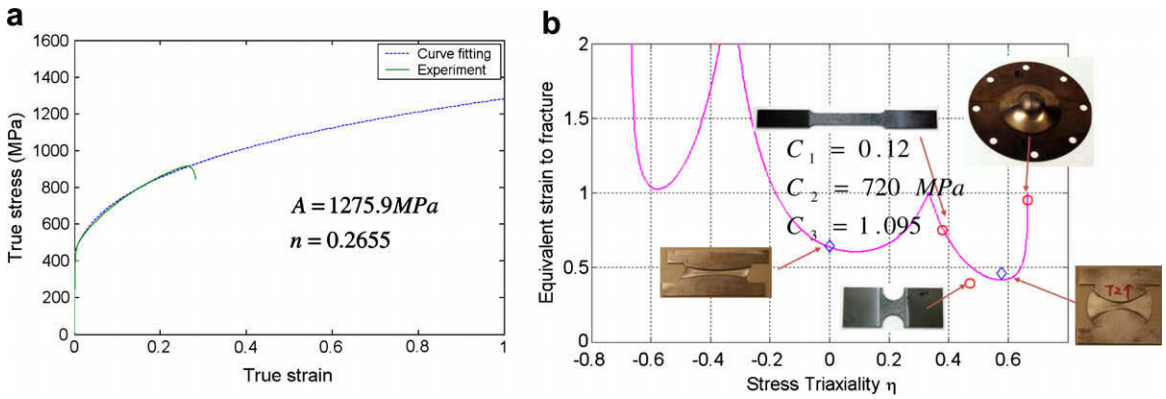

Fig. 3. Experimental calibration of material parameters of TRIP steel. (a) Stress–strain relation for TRIP 690 steel. (b) Fracture parameter calibration (Bai and Wierzbicki, 2010).

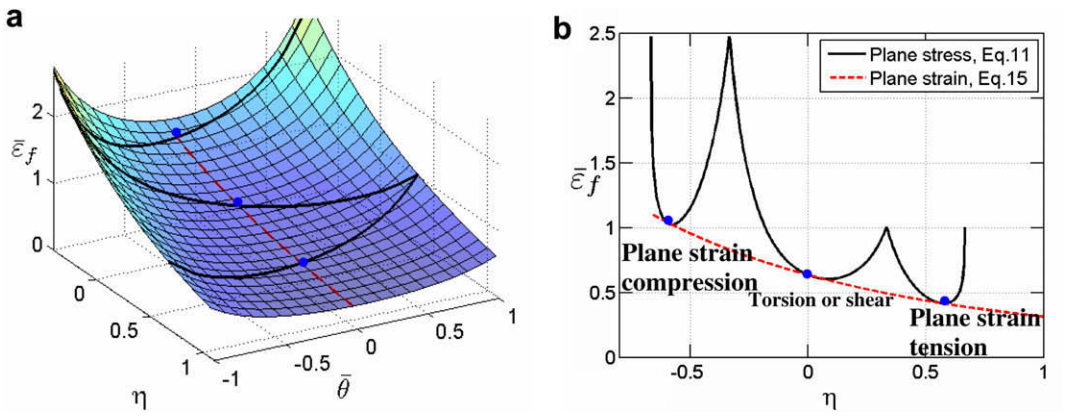

Fig. 4. 3D and 2D triaxiality and lode dependent fracture locus calibrated from Modified Mohr–Coulomb criterion for TRIP steel, plane stress vs. plane strain (a) 3D (Eq. (10)) (b) 2D.

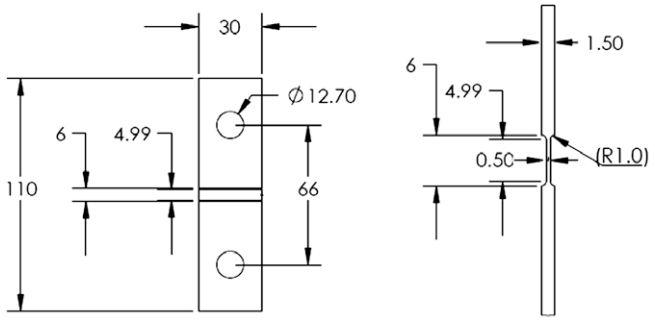

Fig. 5. Dimensions of the flat-grooved tensile specimens of TRIP 690 steel (all dimensions are in mm).

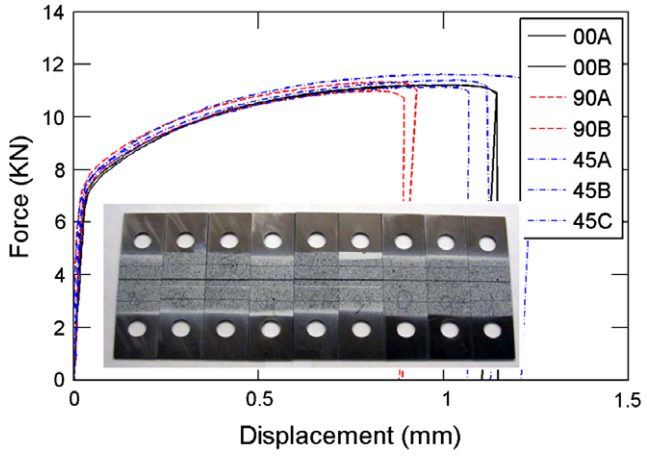

Fig. 6. Experimental load–displacement curves of specimens (solid lines, dash lines and dot-dash lines represent the specimens cut at 0°, 90° and 45° to the rolling direction, respectively; two or three specimens, represented by A, B and C, were made for each material direction).

within the classical plasticity flow theory, it is not possible to predict shear band bifurcation, only diffuse necking can be predicted. In order to capture the slant fracture, it is necessary to introduce either damage or discontinuity to the yield surface. For example, Besson et al. (2003) captured the plane strain slant fracture with both Gurson and Rousselier's constitutive models. But no experiments were conducted to validate this approach. Teng (2008) predict the slant fracture using the CDM approach. A combined implicit-explicit numerical scheme was introduced in Teng's paper to significantly reduce the computational cost for zero or low rate loading process. However, some unacceptable differences were reported between the numerical predictions and the experimental measurement of both fracture load–displacement and strain to failure.

In this section, the semi-coupled method is used to study the plane strain tensile fracture. The damage-induced softening law is proposed, and element deletion is used in simulating post-initiation process. This approach will be verified by the comparison between simulation results and experiments.

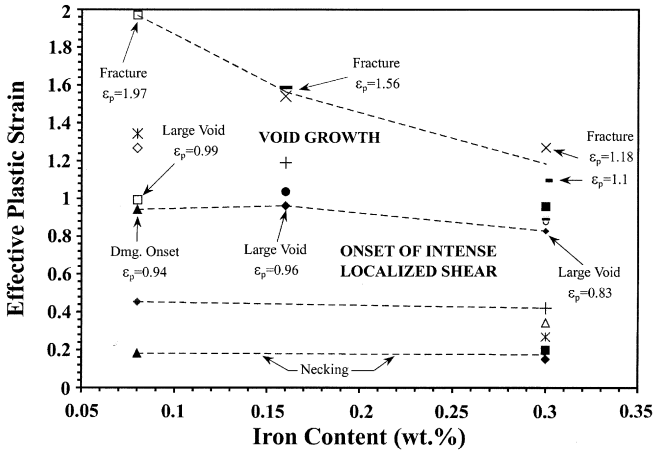

Fig. 7. Relations between necking, initiation of fracture and post-initiation behavior (Spencer et al., 2002).

3.1. Definition of the damage-induced softening

The CDM provides a tool to qualitatively describe the physics of fracture process by define softening due to damage evolution. The mechanisms of damage evolution are complex. In CDM, all the mechanisms are averaged into only one total damage variable D. In the present study, the concept of damage-induced softening is applied. Stress softening is introduced by considering the damage evolution after fracture initiation:

$$\tilde{\sigma}_{flow} = \beta \bar{\sigma}_{flow}, \tag{16}$$

where $\tilde{\sigma}_{flow}$ is the softened flow stress, $\bar{\sigma}_{flow}$ is the original flow stress of the undamaged continuum with no softening. The softening coefficient β is in general nonlinear function of damage. It is assumed here that the softening follows the power law:

$$\beta = \left(\frac{D_c - D}{D_c - D_0}\right)^m, \tag{17}$$

where D_c, D_0 and m are softening parameters need to be determined, and the damage parameter is defined as D. The *damage evolution law* for proportional loading is defined as

$$D = \int_0^{\bar{\varepsilon}_p} \frac{d\bar{\varepsilon}_p}{\bar{\varepsilon}_f(\eta, \bar{\theta})}, \tag{18}$$

where $\varepsilon_f(\eta, \theta)$ is defined by Eq. (10), which is a limiting case of the damage evolution law given by Bai and Wierzbicki (2010).

Therefore, the plastic equivalent stress $\bar{\sigma}_e$ follows:

$$\bar{\sigma}_e = \begin{cases} \bar{\sigma}_{flow} & D \leqslant D_0, \\ \tilde{\sigma}_{flow} & D_0 < D < D_c, \\ 0 & D = D_c. \end{cases} \tag{19}$$

Fracture initiates when $D = D_0$ and $\beta = 1$. A complete separation of the material occurs when $D = D_c$ and $\beta = 0$, after which the material element offers no longer any resistance.

An apparently similar softening rule was proposed by many researchers in the past. However, there is a major difference. In the present theory (Eq. (18)), each damage increment depends not only on the increment of the equivalent strain but also on the stress state through the stress invariants η and $\bar{\theta}$.

The influence of parameters,D_c, and m, on the softening coefficient β is shown in Fig. 8. In a one-dimensional case, the present approach reduces to the cohesive element theory.

3.2. Shear band formation in the material element

The presence of post-initiation softening is a necessary but not sufficient for the slant fracture. The softening parameters introduced in Eq. (17) need to be chosen judiciously to get slant fracture. Material instability in an element triggers slant fracture.

After material instability occurs at a material point/element, shear-band localization follows at the point and propagates to the neighboring points, leading to slant fracture. Thus, the softening parameters in Eq. (17), m, D_c and D_0 should be chosen based on the condition of material instability in an element in the post-initiation state.

Two classes of criteria related to the uniqueness in the local elasoplastic response exist in the existing theoretical system: one is loss of positiveness of second order work of the continuum, which is the sufficient condition for the loss of uniqueness of response $\dot{\underline{\sigma}} : \dot{\underline{\varepsilon}} > 0$ (Hill, 1958). It is based on Drucker's Postulate (Drucker, 1950), and coincides with the condition for vanishing speed of acceleration waves and therefore for strain localization (Hill, 1962); the other is a bifurcation analysis of strain localization, such as Rice (1976). In this study, the former sufficient criterion is used for material instability.

For strain-softening thin sheet in-plane stress ($\dot{\sigma}_3 = 0$) with proportional in-plane loading ($\dot{\sigma}_2 \propto \dot{\sigma}_1$, and $\dot{\varepsilon}_2 \propto \dot{\varepsilon}_1$), the Hill's criterion (1958) can be simplified as the criterion $\frac{d\bar{\sigma}_{flow}}{d\bar{\varepsilon}_p} > 0$.

According to the criterion of material instability, there is a critical value of the damage D_{cr} satisfying Eq. (20), in the post-initiation element. After$D > D_{cr}$, numerically, the damage accumulates to D_c immediately due to the instability and leads to the complete element deletion. In this section, this fact is used to find the range of the softening index m:

$$\left.\frac{d\tilde{\sigma}_{flow}}{d\bar{\varepsilon}_p}\right|_{D=D_{cr}} = 0, \tag{20}$$

where $\bar{\varepsilon}_p$ is the equivalent plastic strain. According to Eq. (16), the total stress is a product of a hardening term $\bar{\sigma}_{flow}(\bar{\varepsilon}_p)$ and a softening term $\beta(D(\bar{\varepsilon}_p))$, therefore:

$$\frac{d\tilde{\sigma}_{flow}}{d\bar{\varepsilon}_p} = \frac{d\beta}{dD}\frac{dD}{d\bar{\varepsilon}_p}\bar{\sigma}_{flow} + \beta\frac{d\bar{\sigma}_{flow}}{d\bar{\varepsilon}_p}. \tag{21}$$

From Eq. (18), we have:

$$\frac{dD}{d\bar{\varepsilon}_p} = \frac{1}{\bar{\varepsilon}_f}, \tag{22}$$

and for a power hardening rule:

$$\bar{\sigma}_{flow} = K\bar{\varepsilon}_p^n. \tag{23}$$

Substituting Eqs. (17), (22) and (23) into Eq. (21) and then Eq. (20), yields:

$$m = n(D_c - D_{cr})\frac{\bar{\varepsilon}_f}{\bar{\varepsilon}_p}. \tag{24}$$

Since $\frac{\bar{\varepsilon}_f}{\bar{\varepsilon}_p} \leqslant 1$, and $D_0 \leqslant D_{cr} \leqslant D_c$, the sufficient condition for a material instability in the post-initiation state and therefore a slant fracture is

$$m \geqslant n(D_c - D_0). \tag{25}$$

Numerical simulations are conducted using plane strain element model, assuming $D_c = 2$, $D_0 = 1$ with different value of m, 0.1, 0.5 and 1. The results are shown in Fig. 9. For $m = 0.1$, Eq. (25) is not satisfied, and there is not enough softening to trigger slant fracture, only flat fracture is obtained. With larger softening parameters $m = 0.5$ and 1, slant fracture can be predicted.

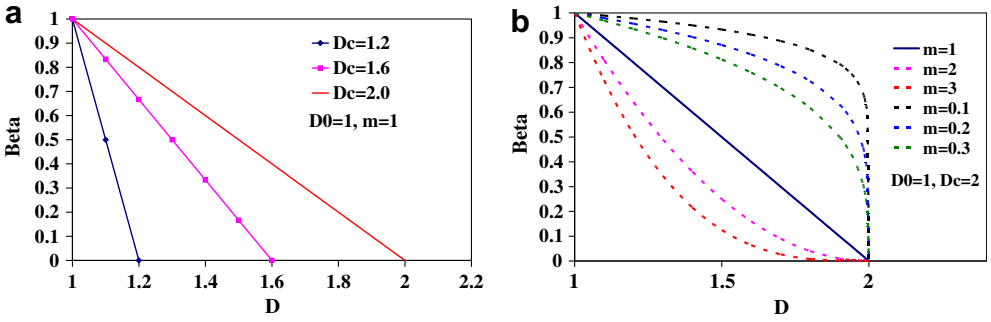

Fig. 8. Parameter study of the damage-induced softening. (a) Influence of D_c. (b) Influence of m.

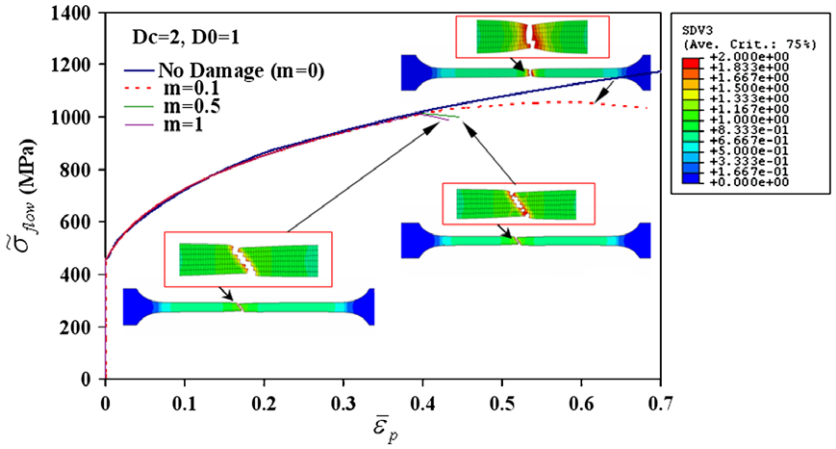

Fig. 9. Influence of m on predicting slant fracture (SDV3 represent the state-dependant-variable: damage D).

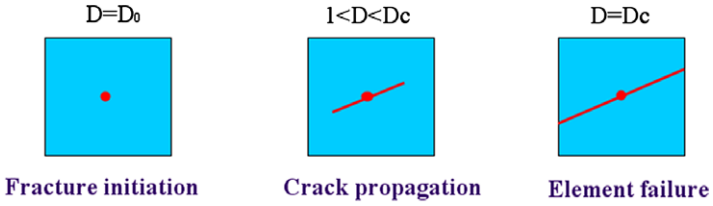

Fig. 10. The concept of the simulation of post-initiation behavior of the element.

3.3. Shear band formation in finite elements

Having explained the softening process at the material level, one can proceed to interpret the softening at the level of a finite element. This is illustrated in Fig. 10.

Fracture is assumed to initiate when $D = D_0$ at one point within an element. Because of a finite size of the element, some additional work is needed to propagate the crack through the element. The work is supplied by release of the elastic strain energy in the surrounding elements or by the controlled displacements. The element is gradually losing it strength until a total separation occurs at$D = D_c$. The above interpretation of the "structural" softening has laid to a very realistic description of the fracture process, including the prediction of slant fracture. It is believed that the damage indicator, defined by Eq. (18) is an alternative choice for characterizing the amount of damage within a finite element besides the relative displacement approach, as proposed in ABAQUS manual (ABAQUS, 2008). Both approaches can partially remove the mesh size effect.

We should see now how the proposed method works to simulate plane strain fracture. A conceptual sketch illustrating the process of flat fracture vs. slant fracture is shown in Fig. 11, in which, the first element to reach the critical value D_c and to be deleted is located at the center of a cross section. A competition of reaching the critical value D_c first is carried out between the two neighboring elements '2' and '3'. The element '2' is located at the horizontal axis of symmetry while the element '3' is positioned diagonally. Two scenarios may develop, as illustrated in Fig. 11.

The deletion of element 2 is more likely to trigger the symmetric crack propagation, which will lead to a flat fracture. The deletion of element 3 on the other hand is more likely to trigger the anti-symmetric fracture mode, which will lead to a slant fracture. Also, the damage evolution for critical elements (elements in the center, elements 2 and 3) at critical stages (a, b, c, d and e) are shown in Fig. 11. Stage a represents the fracture initiation with the formation of a crack tip in the center. The critical step in determining which element will be deleted next, (thus defining the direction of the crack propagation) is a transition from stage a to

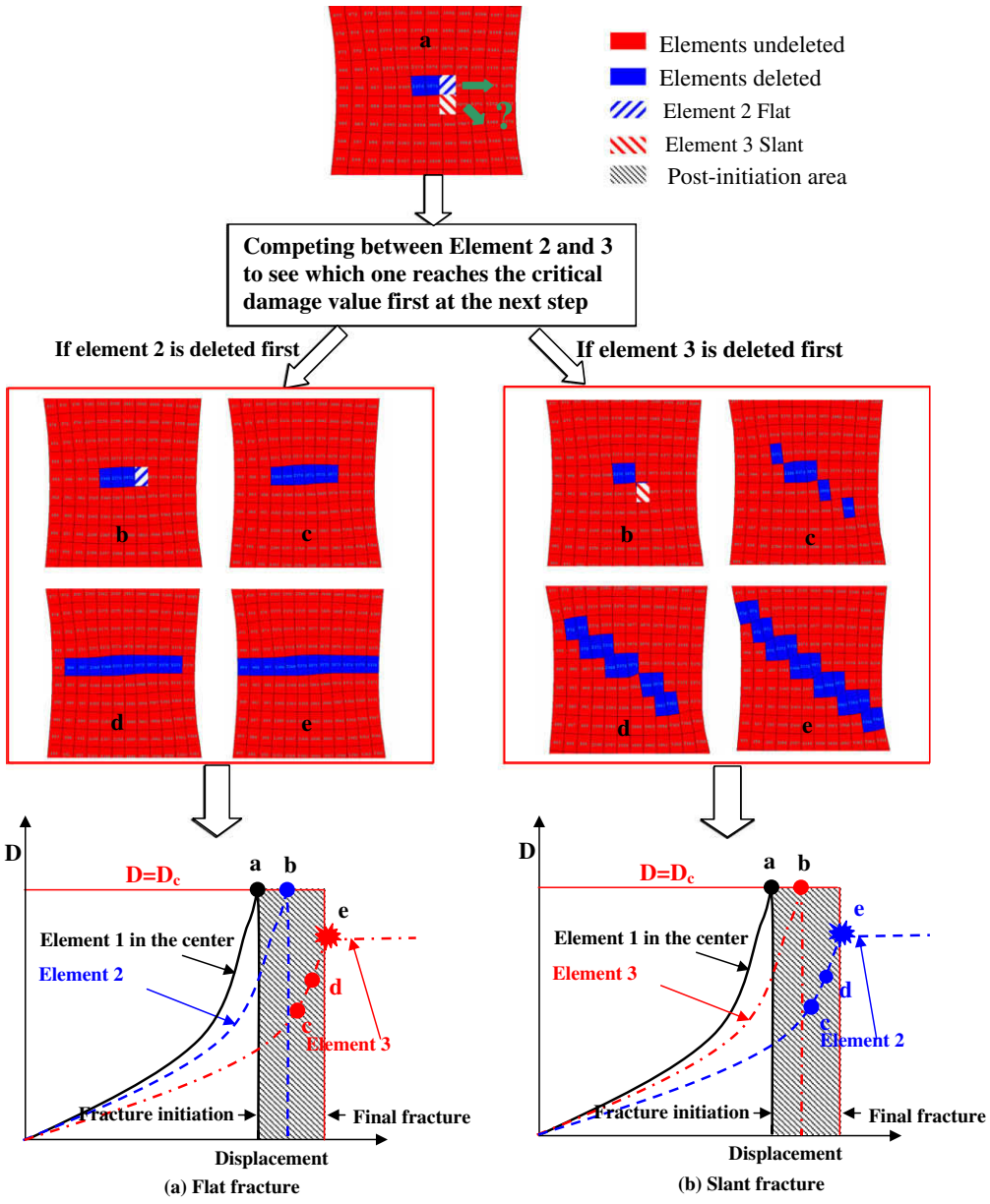

Fig. 11. A conceptual sketch of flat fracture evolution vs. slant fracture evolution.

stage b. Stage c and d represent either stable or unstable propagation of the crack. Stage e represents the final fracture of the cross section, which means the separation of the plane strain specimen, when the final fracture displacement is reached.

4. Parametric study

Several factors may influence the path of a crack. These are element size, initial element aspect ratio, element type, and the magnitude of softening parameters m. The objective of this section is to capture slant fracture efficiently by optimizing these factors. Shell element model is unable to capture the slant fracture through thickness and solid element models are computationally expensive for parametric study. Therefore, plain strain element model are used for all of the following simulations in this section. All fracture simulations were conducted for fixed values of the damage parameters $D_0 = 1$, $D_c = 1.2$. One factor is changed at a time in the following subsections.

4.1. Effect of initial element aspect ratio (EAR)

In this section, $m = 1$ is used. The initial element aspect ratio is defined by (EAR = W/H), where W is the width of the element through the thickness of the specimen and H equals to the length of the element in the major loading direction. Two aspect ratios are considered: 1 and 4. It is shown in Fig. 12 that the EAR has little influence on the fracture load–displacement, but the slant fracture mode is more easily to be predicted by a larger initial EAR.

The mechanisms of flat fracture vs. slant fracture were shown conceptually in Fig. 11. Herein, the real computational results of damage evolutions of critical elements are compared in Fig. 13. The two mechanisms are proved by comparing Fig. 13 with Fig. 11.

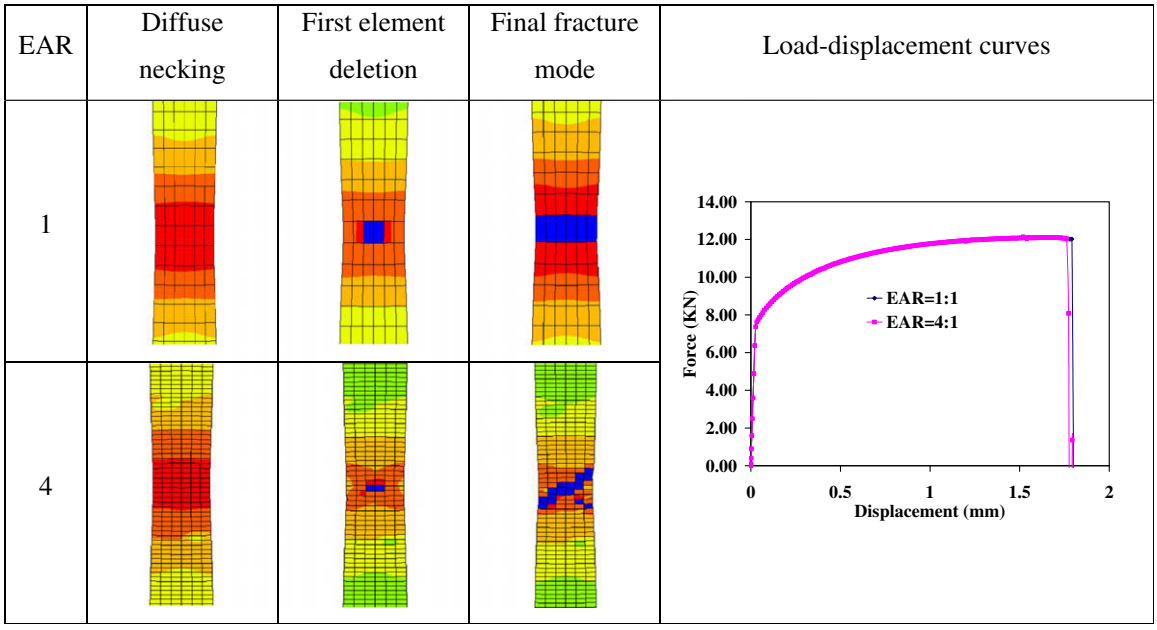

Fig. 12. Influence of element aspect ratio (EAR).

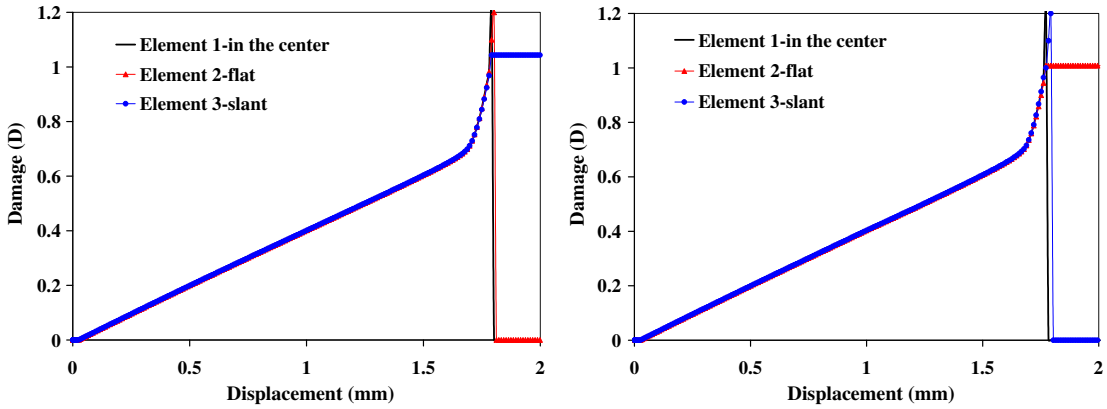

Fig. 13. Damage evolution for different EAR (the definition of element 1, 2 and 3 refers to Fig. 12).

The study above demonstrates that the mesh size in the major loading direction is more important for predicting slant fracture than the mesh size in the transverse direction. If the mesh size in the loading direction is large and comparable with the size of the diffused localization zone, the slant fracture can not be predicted, which is worth noting in mesh optimization.

4.2. Effect of element type

Two different types of elements are used for simulations. One is 4-node rectangular plane strain element CPE4 in ABAQUS, the other is the 3-node triangular element CPE3 in ABAQUS. The mesh sizes of both are the same.

It is shown in Fig. 14 that the triangular element model predicts the slant fracture while the rectangular element model shows the flat fracture. Part of the reason is that the triangular mesh is more isotropic, while the rectangular mesh is orthotropic, which indicates that when simulating crack propagation, the triangular mesh has no preference of separation in any direction, while the rectangular mesh tends to separate in orthogonal directions, thus is more likely to cause a flat fracture. In addition, the triangular element is more realistic to represent the diamond shape of macro void formed in the center shown by Spencer et al. (2002).

4.3. Effect of mesh size

In this subsection, different mesh sizes are used in the FE simulations: 0.08, 0.04 and 0.02 mm representing 6, 12 and 24 elements through thickness, respectively. The initial EARs of all the elements are all equal to 1. $m = 1$ is used as before.

It can be seen from Fig. 15 that the load–displacements are almost mesh size independent. Part of the reason is that the fracture occurs before the localized necking in the simulation. The first element deleted helps trigger the shear band localization if the size of the element is smaller than the size of the potential shear band. If not, a flat fracture mode will form, as shown in Fig. 15.

4.4. Effect of softening parameter m

In this section, the influence of the nonlinearity of the softening process, quantified by the exponent m is studied. It is well known that softening is necessary for predict slant fracture. With no soft-

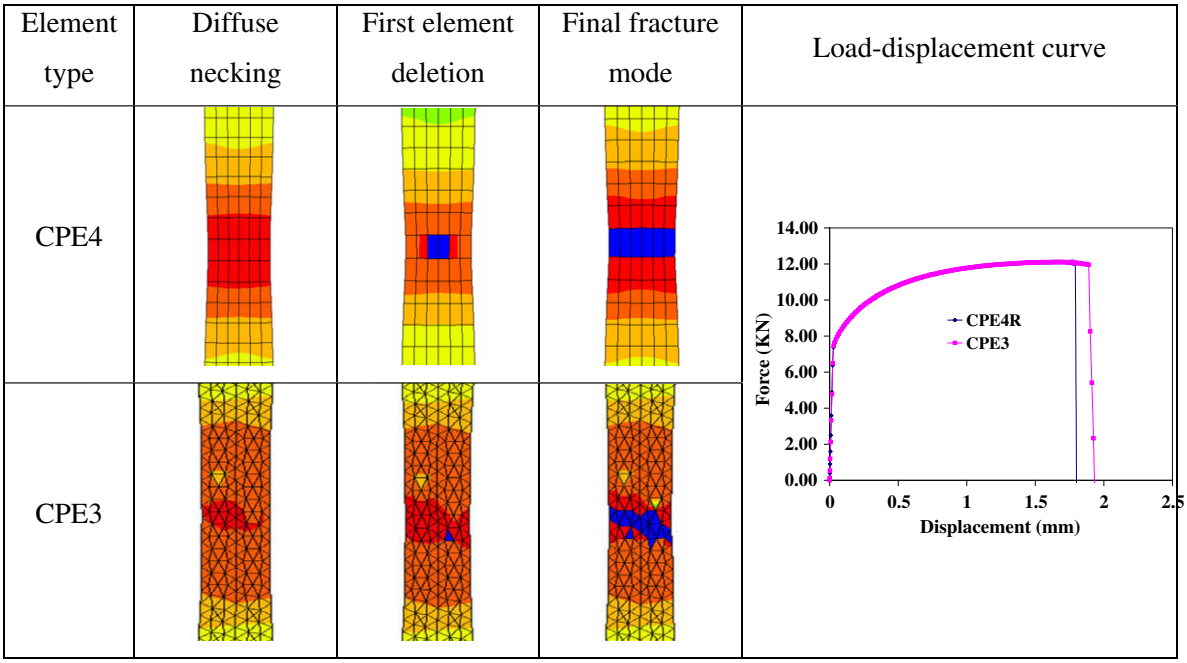

Fig. 14. Influence of the element type.

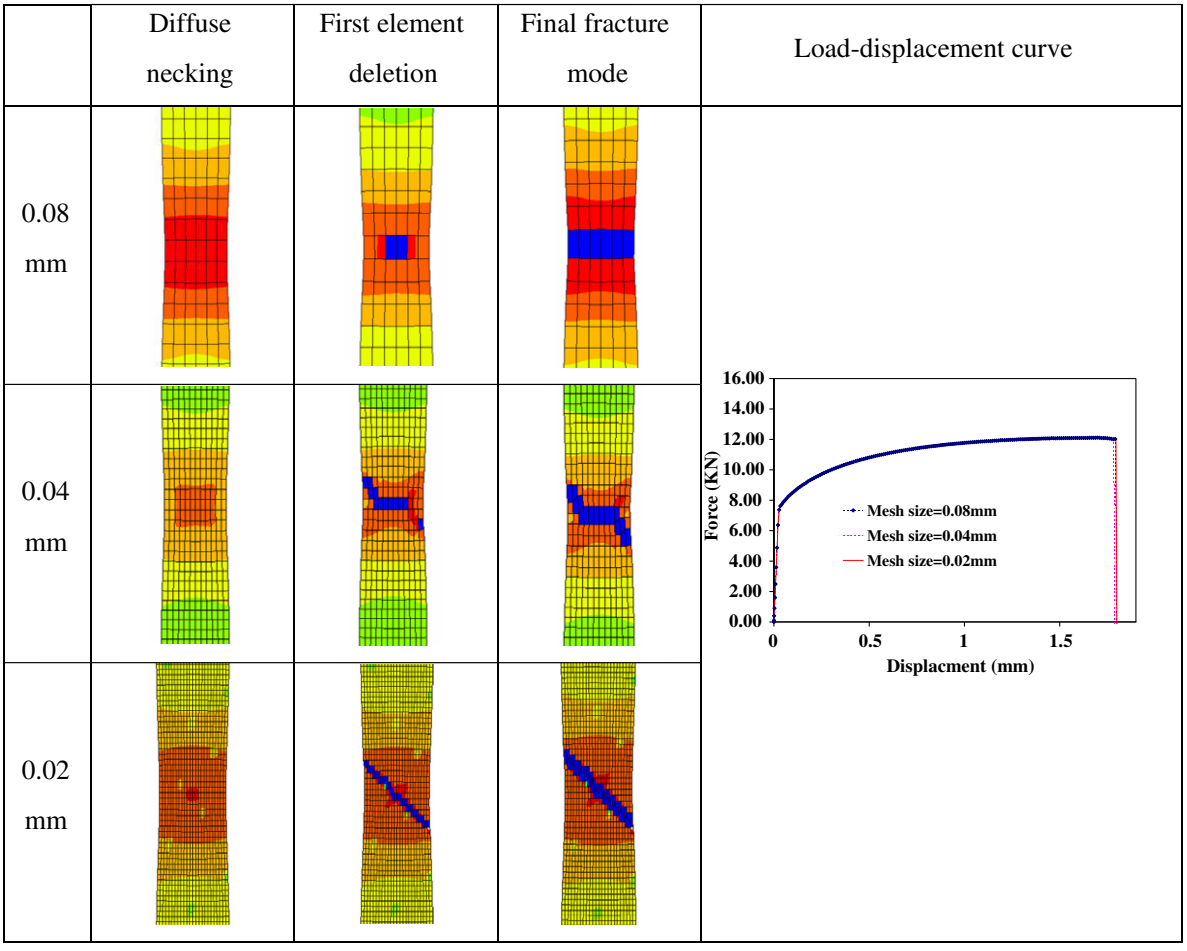

Fig. 15. Influence of mesh size.

ening, no slant fracture can be predicted in the simulations. The softening parameter needs to be chosen judiciously to predict slant fracture. Details were demonstrated in Section 3.2. It is shown again in Fig. 16 that a larger softening parameter m predicts the

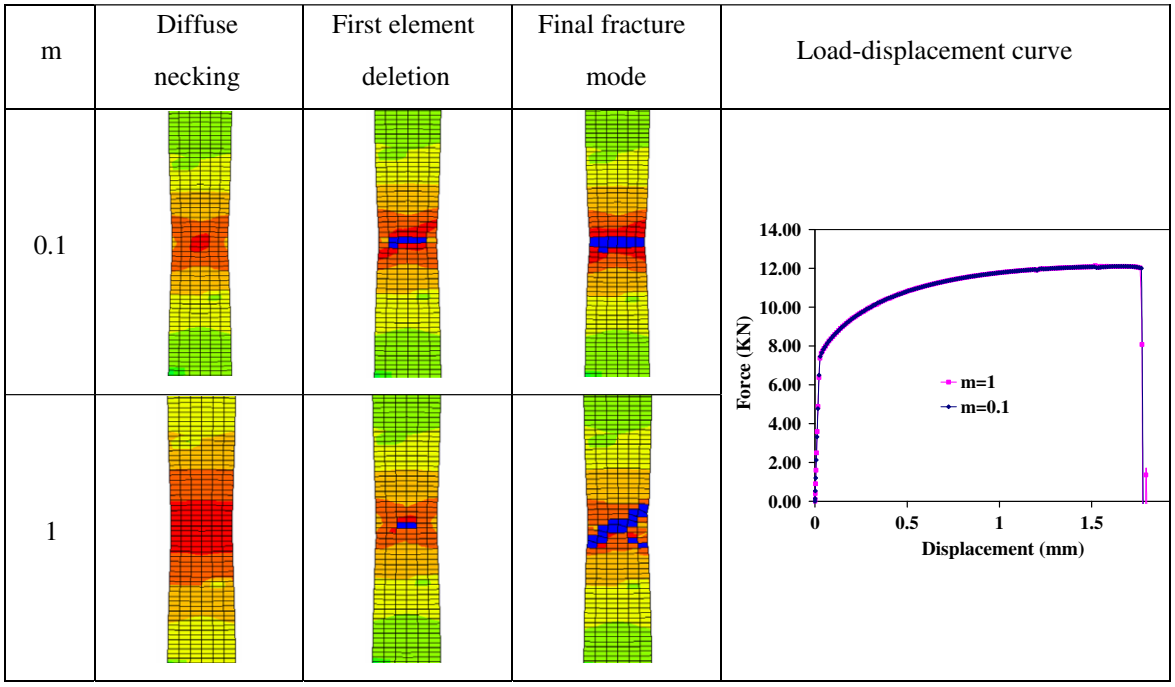

Fig. 16. Influence of *m*.

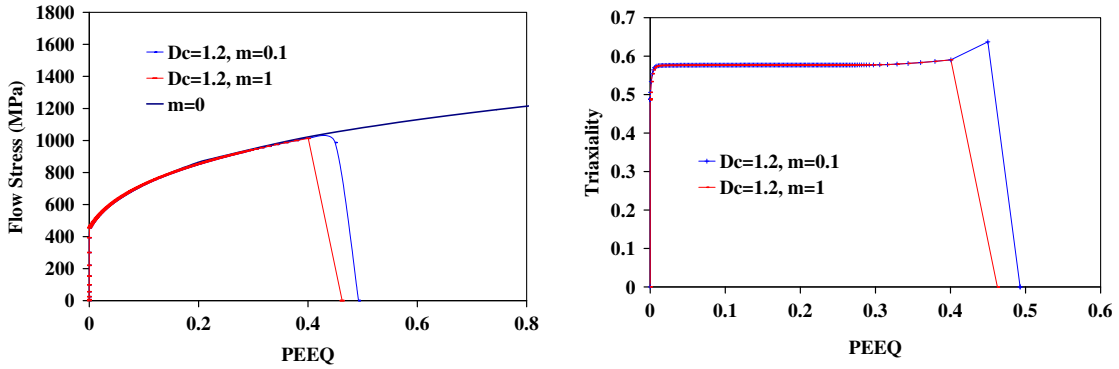

Fig. 17. The *m*-dependency of the history of the state variables at the critical element.

slant fracture while a smaller one predicts the flat fracture. Thus, for larger *m* it is easier to form slant fracture than for smaller exponent.

The histories of the state variables at the center element were monitored. The histories of the flow stress and the triaxiality of the center element are plotted and compared in Fig. 17. Before fracture initiates, the triaxiality in the center is a constant. Right after fracture initiates, the triaxiality increases. This increment is due to the vanishing stress in a post-initiate element.

As shown in Fig. 17, for larger *m*, the first element is deleted more rapidly, no time is left for the damage propagation horizontally and the first element deletion helps the shear band formation and therefore the slant fracture. For smaller *m*, the element in the center is deleted slowly, more time is left for the horizontal damage propagation and therefore the flat fracture.

4.5. Partial summary

The parametric study provided a deeper insight into the formation of slant fracture. Generally, with a finer mesh size is easier to trigger slant fracture than a coarse mesh. The mesh size in the loading direction has more influence on triggering slant fracture. Therefore, larger EAR is preferred in the loading direction. With tri-

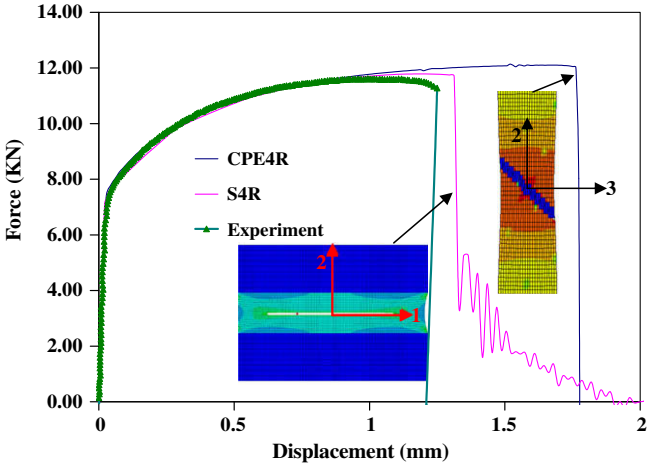

Fig. 18. Comparison of experimental and prediction results.

angular elements it is easier to trigger slant fracture since there is no directional preference. The rectangular elements have more orthogonal direction oriented preference. The softening exponent m needs to be large enough to trigger slant fracture.

5. Discussion

Fig. 18 shows the comparison of load–displacement curves of plane strain element (CPE4R) model, the shell element model and the experiments. The details of the simulations using shell element (S4R in ABAQUS) model can be found in Li and Wierzbicki (2009). The shell element model is mesh size dependent (Li and Wierzbicki, 2009). In Fig. 18, the curve of the shell element model with mesh size 0.25 mm is shown, and the curve of the plane strain element model is with mesh size 0.02 mm. Experiment results of the flat-grooved specimens show machining-induced anisotropy, although the material is isotropic, as shown in Fig. 6. In Fig. 18, only one curve with the largest fracture displacement in Fig. 6 is shown to represent the experimental results. Discrepancies exist among these results. The reasons for these discrepancies are discussed in this section.

First, it can be seen from Fig. 18 that results of both shell element model and plane strain element model over-predict the fracture displacement, although the result of shell element model is closer to the experimental data. This is because the initial imperfections of the specimens caused by the machining. The thickness of the flat-grooved part of the speciment is only 0.5 mm. The machining process of the thin sheets is more likely to introduce much larger initial imperfection than thicker sheets. However, in the simulations, all the models are initially perfect.

Second, fracture displacement predicted by the plane strain element model is larger than that of shell element model. The main reason for this discrepancy is that the assumption of plane strain condition when using plane strain element model is not strictly satisfied for these specimens. As shown in Fig. 5, the width of the specimen is 30 mm, the length of the flat-grooved part is about 5 mm. Compared with shell element model and real specimens, plane strain element model is over-constrained. The over-constrained boundary conditions lead to the over-prediction of the fracture displacement.

However, the less accurate predicted fracture displacement of plane strain element model should not reduce the value of the present investigation. The results of shell element model is mesh size dependent, by choosing the mesh size judiciously and considering the initial imperfection, the shell element model should be able to capture the experimental load–displacement curve accurately. But, the shell element model is not able to predict the slant fracture through thickness. The results of plane strain element model converge with the refined mesh, as shown in Section 4.3, and can capture the slant fracture through thickness. Solid element model has the advantages of both shell element model and plane strain element model. But, it is computationally expensive and thus is not suitable for a parametric study. Therefore, plane strain element model is chosen to study slant fracture and post-initiation behavior, although the load–displacement prediction result is less satisfactory due to the reasons mentioned in the above paragraph. By applying conclusions obtained from this investigation, an example of very accurate prediction of slant fracture using solid elements in the combined Mode I/III crack propagation of Al6061-T6 is given by Li et al. (2010). Accurate load–displacement curves, displacements to fracture and slant fractures can be obtained.

6. Conclusions

In this paper, the semi-coupled plasticity/fracture model is used to predict ductile fracture for flat-grooved plane strain tensile specimen of TRIP 690 steel. The initiation of fracture is assumed to be governed by the three-parameter Modified Mohr–Coulomb fracture model. Then, the post-initiation behavior is simulated by introducing a new type of the damage-induced softening. VUMAT subroutines of ABAQUS are connected with ABAQUS/EXPLICIT to simulate the post-initiation process of elements. Element deletion is used to simulate the crack propagation. A specific form of softening law is proposed. It is shown that the softening is crucial to simulate slant fracture through thickness which is always observed in thin sheets. Plane strain element model can predict slant fracture by simulating the post-initiation behavior. Different factors influencing the slant fracture mode such as the amount of softening, element design and element mesh sizes were identified and studied.

Acknowledgements

Thanks are due to Dr. Yuanli Bai, Dr. Xiaoqing Teng and Professor Lallit Anand at MIT for their valuable comments. The authors gratefully appreciate the financial support from the AHSS MIT industry consortium.

References

ABAQUS, 2008. User's Manual, Version 6.8, Hilbbit, Karlsson and Sorensen Inc.
Bai, Y., 2008. Effect of Loading History on Necking and Fracture, Ph.D. Thesis, Massachusetts Institute of Technology.
Bai, Y., Wierzbicki, T., 2008. A new model of metal plasticity and fracture with pressure and Lode dependence. International Journal of Plasticity 24, 1071–1096.
Bai, Y., Wierzbicki, T., 2010. Application of extended Mohr–Coulomb criterion to ductile fracture. International Journal of Fracture 16, 1–20.
Bao, Y., Wierzbicki, T., 2004a. A comparive study on various ductile crack formation criteria. Journal of Engineering Materials and Technology 126, 314–324.
Bao, Y., Wierzbicki, T., 2004b. On fracture locus in the equivalent strain and stress triaxiality space. International Journal of Mechanical Sciences 46, 81–98.
Bao, Y., Wierzbicki, T., 2005. On the cut-off value of negative triaxiality for fracture. Engineering Fracture Mechanics 72 (7), 1049–1069.
Beese, A., Luo, M., Li, Y., Bai, Y., Wierzbicki, T., 2010. Partially coupled anisotropic fracture model for aluminum sheets. Engineering Fracture Mechanics 77, 1128–1152.
Besson, J., Steglich, D., Brocks, W., 2001. Modeling of crack growth in round bars and plane strain specimens. International Journal of Solids and Structures 38, 8259–8284.
Besson, J., Steglich, D., Brocks, W., 2003. Modeling of plane strain ductile rupture. International Journal of Plasticity (19), 1517–1541.
Chaboche, J.L., 1981. Continuous damage mechanics: a tool to describe phenomena before crack initiation. Nuclear Engineering and Design 64, 233–247.
Coleman, B.D., Gurtin, M.E., 1967. Thermodynamics with internal state variables. Journal of Chemical Physics 47, 597–613.
Drucker, D.C., 1950. Some implications of work hardening and ideal plasticity. Quarterly of Applied Mathematics 7, 411–418.
Gurson, A.L., 1975. Plastic Flow and Fracture Behavior of Ductile Materials Incorporating Void Nucleation, Growth and Interaction. Brown University.
Gurson, A.L., 1977. Continuum theory of ductile rupture by void nucleation and growth: part I- yield criteria and flow rules for porous ductile media. Transactions of the ASME – Journal of Engineering Materials and Technology.
Hill, R., 1958. A general theory of uniqueness and stability in elastic-plastic solids. Journal of the Mechanics and Physics of Solids 6, 236.
Hill, R., 1962. Acceleration waves in solids. Journal of the Mechanics and Physics of Solids 10, 1–16.
Hosford, W.F., 1972. A generalized isotropic yield criterion. Journal of Applied Mechanics 39, 607–609.
Hult, J., 1979. Continuum Damage Mechanics – Capabilities Limitations and Promises, Mechanics of Deformation and Fracture. Pergamon, Oxford. pp. 233–247.
Hutchinson, J.W., Tvergaard, V., 1981. Shear band formation in plane strain. International Journal of Solids and Structures 17, 451–470.
Kachanov, L.M., 1958. Time of the rupture process under creep conditions. Izvestiya Akademii Nauk SSSR. Otdelenie Teckhnicheskikh Nauk 8, 26–31 (in Russian).
Krajcinovic, D., 1984. Continuum damage mechanics. Applied Mechanics Review 37 (1), 1–6.
Lemaitre, J., 1985. A continuous damage mechanics model for ductile fracture. Journal of Engineering Materials and Technology 107, 83–89.
Li, Y., Wierzbicki, T., 2009. Mesh-size study of ductile fracture by non-local plasticity model. In: Proceeding of SEM Annual Conference and Exposition on Experimental and Applied Mechanics, June 2009, Paper No. 387, Albuquerque.

Li, Y., Wierzbicki, T., Sutton, M., et al. 2010. Mixed mode stable tearing of thin sheet Al6061-T6 specimens: experimental measurements and finite element simulations using a Modified Mohr–Coulomb fracture criterion, International Journal of Fracture, submitted for publication.

McClintock, F.A., 1968. A criterion for ductile fracture by the growth of holes. Journal of Applied Mechanics, 363–371.

Rice, J.R., 1971. Inelastic constitutive relations for solids: an internal-variable theory and its application to metal plasticity. Journal of the Mechanics and Physics of Solids 19, 433–455.

Rice, J.R., 1976. The localization of plastic deformation. In: Koilter, W.T. (Ed.), Theoretical and Applied Mechanics. North-Holland, Amsterdam, p. 207.

Rice, J.R., Tracey, D.M., 1969. On the ductile enlargement of voids in triaxial stress fields. Journal of the Mechanics and Physics of Solids 17, 201–217.

Spencer, K., Corbin, S.F., Lloyd, D.J., 2002. The influence of iron content on the plane strain fracture behaviour of AA 5754 Al–Mg sheet alloys. Materials Science and Engineering A325 (1-2), 394–404.

Teng, X., 2008. Numerical prediction of slant fracture with continuum damage mechanics. Engineering Fracture Mechanics 75 (8), 2020–2041.

ThyssenKrupp Auto Division-Product Overview, 2008. ThyssenKrupp Steel Europe AG, Duisburg, Germany.

Wierzbicki, T., Xue, L., 2005. On the Effect of the Third Invariant of the Stress Deviator on Ductile Fracture. Technical Report. Impact and Crashworthiness Laboratory, Massachusetts Institute of Technology, Cambridge, MA.

Xue, L., 2007. Damage accumulation and fracture initiation in uncracked ductile solids subject to triaxial loading. International Journal of Solids and Structures 44, 5163–5181.